Journal Pre-proof

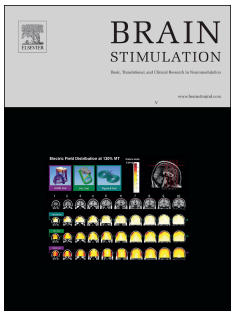

Non-invasive optogenetics with ultrasound-mediated gene delivery and red-light excitation

Antonios N. Pouliopoulos, Maria F. Murillo, Rebecca Lynn Noel, Alec Batts, Robin Ji, Nancy Kwon, Han Yu, Chi-Kun Tong, Jennifer N. Gelinas, Dion Khodagholy Araghy, S. Abid Hussaini, Elisa E. Konofagou

PII: S1935-861X(22)00111-5

DOI: https://doi.org/10.1016/j.brs.2022.06.007

Reference: BRS 2205

To appear in: *Brain Stimulation*

Received Date: 18 April 2022

Revised Date: 30 May 2022

Accepted Date: 11 June 2022

Please cite this article as: Pouliopoulos AN, Murillo MF, Noel RL, Batts A, Ji R, Kwon N, Yu H, Tong C-K, Gelinas JN, Araghy DK, Hussaini SA, Konofagou EE, Non-invasive optogenetics with ultrasound-mediated gene delivery and red-light excitation, *Brain Stimulation* (2022), doi: https://doi.org/10.1016/j.brs.2022.06.007.

Non-invasive optogenetics with ultrasound-mediated gene delivery and red-light excitation

Credit author statement

A.N.P., S.A.H. and E.E.K. conceived the concept and designed the experiments. A.N.P. performed the experiments and analyzed the data; M.F.M. and N.K. performed the immunohistochemistry. S.A.H. performed the in vivo electrophysiology measurements. H.Y., J.N.G. and D.K.A. performed the multi-electrode array recordings. C.K.T. performed the Ca2+ imaging. M.F.M. performed the fear conditioning experiment. All authors discussed the results and approved the manuscript.

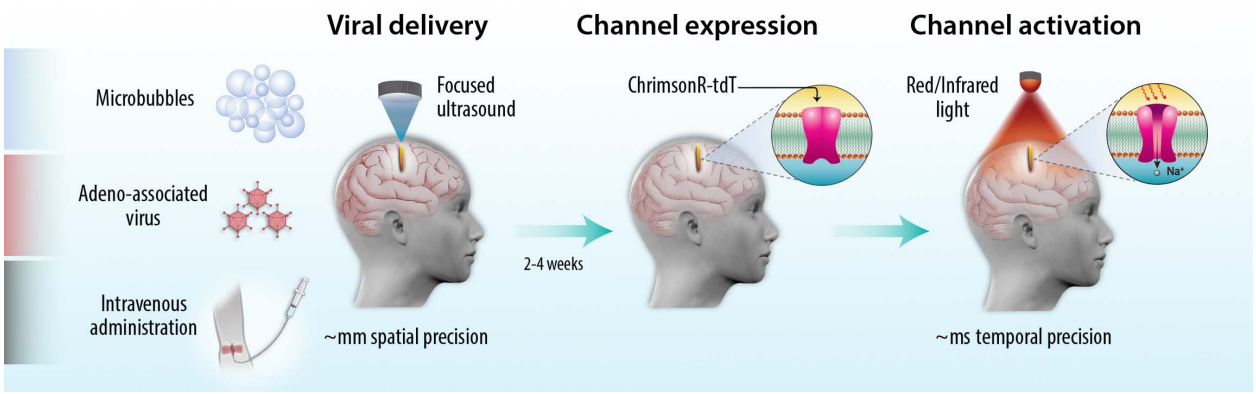

Non-invasive optogenetics with ultrasound-mediated gene delivery and red-light excitation

Antonios N. Pouliopoulos[a,1], Maria F. Murillo[a], Rebecca Lynn Noel[a], Alec Batts[a], Robin Ji[a], Nancy Kwon[a], Han Yu[b], Chi-Kun Tong[c], Jennifer N. Gelinas[d], Dion Khodagholy Araghy[b], S. Abid Hussaini[e], Elisa E. Konofagou[a,f,*]

a. *Department of Biomedical Engineering*

b. *Department of Electrical Engineering*

c. *Department of Physiology and Cellular Biophysics*

d. *Department of Neurology*

e. *Department of Pathology and Cell Biology*

f. *Department of Radiology*

Columbia University, New York City, NY, USA

[1]Current address: Department of Surgical & Interventional Engineering, King's College London, London, UK

* Corresponding author: Elisa E. Konofagou, ek2191@columbia.edu

Abstract

Optogenetics has revolutionized the capability of controlling genetically modified neurons *in vitro* and *in vivo* and has become an indispensable neuroscience tool. Using light as a probe for selective neuronal activation or inhibition and as a means to read out neural activity has dramatically enhanced our understanding of complex neural circuits. However, a common limitation of optogenetic studies to date is their invasiveness and spatiotemporal range. Direct viral injections into the brain tissue along with the implantation of optical fibers and recording electrodes can disrupt the neuronal circuitry and cause significant damage. Conventional approaches are spatially limited around the site of the direct injection and insufficient in examining large networks throughout the brain. Lastly, optogenetics is currently not easily scalable to large animals or humans. Here, we demonstrate that optogenetic excitation can be achieved entirely non-invasively through the intact skull in mice. Using a needle-free combination of focused ultrasound-mediated viral delivery and extracorporeal illumination with red light, we achieved selective neuronal activation at depths up to 4 mm in the murine brain, confirmed through cFos expression and electrophysiology measurements within the treated areas. Ultrasound treatment significantly reduced freezing time during recall in fear conditioning experiments, but remote light exposure had a moderate effect on the freezing behavior of mice treated with viral vectors. The proposed method has the potential to open new avenues of studying, but also stimulating, neuronal networks, in an effort to elucidate normal or dysfunctional brain activity and treat neurological diseases. Finally, the same non-invasive methodology could be combined with gene therapy and applied to other organs, such as the eye and the heart.

Introduction

Genetically modifying neurons to render them responsive to external stimuli has enabled interaction with the brain at subcellular, cellular and circuit levels. Introduction of thermally- (e.g., TRPV1), chemically- (e.g. DREADDs), acoustically- (e.g., mPrestin), and optically-activated (e.g., channelrhodopsin) ion channels into specific neuronal circuits has led to the development of magnetogenetics [1], chemogenetics [2], sonogenetics [3,4], and optogenetics [5], respectively. Optogenetics was firstly introduced by Boyden et al. in 2005 [5], and has since transformed the way neuronal activity is instigated and detected, both *in vitro* and *in vivo*, becoming the most widely used technique for neuronal control [6,7].

A typical optogenetic experiment *in vivo* involves the direct injection of a viral vector encoding the light-sensitive ion channel channelrhodopsin (ChR2) into the brain region of interest. Following a period of a few weeks to allow for viral transduction and channel expression, an optical fiber is implanted into the same region and delivers blue light pulses to optically activate the newly expressed Na^+ channels. Neuronal activity is typically recorded using implanted electrodes [8,9]. This process can be conducted in several brain regions, elucidating circuits responsible for functions such as perception [10], memory retrieval [11], emotional valence [12], or fear recall [13,14].

Despite its tremendous success over the past two decades, conventional optogenetics is restricted by important limitations. Direct injections and fiber/electrode implantations are invasive and may lead to significant tissue damage and morbidity. The neural networks being studied are therefore subject to violation, and potentially detrimental functional changes. Furthermore, the blue light typically used has limited tissue penetration (< 1% at 1 mm distance [15]) and is confined within a small volume around the fiber tip. Finally, the vast majority of optogenetic studies have been conducted in rodents, which allow for direct injections in multiple areas due to the brain size and relative simplicity of neural projections. However, scaling of this technique to larger animals (e.g., primates) or humans is challenging, due to the size and depth of the respective brain circuits.

To address these limitations, a variety of red-shifted opsins has been developed [16–18]. Red light (λ ~ 620-700 nm) is less scattered by the skull and tissues, and is absorbed less by blood, rendering it more

favorable than blue light for transcranial stimulations. Near infrared (λ ~ 1 μm) illumination of upconversion nanoparticles has been implemented to transcranially produce visible light and optogenetic excitation at depths up to 5 mm [19]. These opsins were thus far introduced with direct injections into the brain regions under evaluation. Recently, chimeric AAV-PHP vectors were designed to cross the BBB and transduce specific neuronal types (e.g., raphe nuclei or Purkinje neurons) [20]. This approach enables non-invasive stimulation of neuronal sub-types, but has limited spatial control over complex neuronal circuits. In previous work, we and others have replaced the direct injection of viral vectors with focused ultrasound (FUS)-mediated viral delivery [21]. We have shown that optogenetic activation of blue-sensitive ChR2 was possible following intravenous administration of adeno-associated virus (AAV) and targeted gene delivery across the blood-brain barrier (BBB), using a combination of FUS and circulating microbubbles [22]. Another FUS-based approach involves the use of mechanoluminescent nanoparticles, which can be charged in superficial vessels by 400-nm photoexcitation light and activated with FUS in the targeted area, emitting 470-nm light [23]. This approach was demonstrated in transgenic ChR2 mice, but in principle requires direct injection of viral vectors for wild-type animals and has the limitation of using blue light for activation, restricting the range and uniformity of neuronal excitation within the vicinity of brain blood vessels.

Here, we performed non-invasive and localized delivery of a systemically administered AAV9-encoded red-shifted opsin variant into the mouse brain, which was then transcranially activated with red light. Neuronal activation within the targeted and neighboring areas was established with a multitude of electrophysiology techniques. Finally, we studied the long-term freezing behavior of animals treated with FUS +/- AAV, to evaluate the ability of non-invasive optogenetics to influence complex behaviors in a non-invasive, selective and safe manner.

Results

Non-invasive optogenetics method

Non-invasive optogenetics with FUS-mediated gene delivery and red-light activation is a two-step process (Fig. 1a, concept illustration). The channel-encoding viral vector (e.g., AAV) is first intravenously co-administered with pre-formed microbubbles, which are subsequently activated by the FUS field. Microbubble volumetric oscillations within the focal volume (~ mm in diameter) exert mechanical forces onto surrounding vascular walls, transiently opening the BBB at the targeted location. The light-sensitive channel (e.g., ChrimsonR [24]) used here is expressed within a period of weeks, before being transcranially activated with red light. The targeted FUS-mediated BBB opening allows viral delivery at ~ mm spatial precision even at ~ cm depths [21]. Channel activation can be achieved at ~ ms temporal precision, with red light pulses at kHz rates.

Here, we implemented the proposed technique in a mouse model (Fig. 1b). We used a pre-clinical FUS system described elsewhere [25,26], to open the BBB and deliver the AAV in anesthetized mice fixed within a stereotaxic frame. The emission system included a 1.5-MHz FUS transducer, emitting 0.8-MPa ultrasonic pulses at a 5 Hz rate. Microbubble emissions stemming from cavitation activity were monitored in real-time through passive cavitation detection (PCD), to characterize the cavitation response during treatment and evaluate the safety of BBB opening. Following a period of at least 3 weeks, mice were exposed to red light using a 635-nm LED to elicit neuronal activation. The dimensions of the ellipsoidal focal volume of the 1.5-MHz FUS transducer, measured in free field with a bullet hydrophone, were 1 mm × 1 mm × 7.5 mm (Fig. 1c). These dimensions ensured accurate control of BBB opening and viral delivery along the transverse plane, with a less confined delivery along the axial direction. On the other hand, the divergent LED beam had a transverse full-width-at-half-maximum (FWHM) of ~ 8 mm (Fig. 1d) and was selected to illuminate the entire surface of the murine brain. Due to beam divergence, the light intensity dropped to 50% of the emitted intensity 23 mm away from the LED surface.

Light propagation model

To determine the depth threshold of channel activation, we analytically calculated the light intensity or irradiance over depth in a three-compartmental model of air, skull, and brain (Fig. 1e). The transmission coefficient of each compartment was measured with a digital photometer from *ex vivo* samples of excised mouse skull and brain tissue, and then inserted into the model developed by Aravanis et al. [15]. The transmission coefficients for air, skull, and brain, were measured as 1, 0.14, and 0.125, respectively. The refractive indices at 635 nm were estimated at 1, 1.53, and 1.36, respectively. The numerical aperture of the LED source was 0.122. Finally, the half angles were 7º, 4.6º, and 5.1º, respectively. The average skull thickness across the illuminated area, measured with a caliper, was 0.3 mm.

We modeled two scenarios, one with (Fig. 1f) and the other without (Fig. 1g) the skull in place, i.e., following craniotomy. The skull caused substantial attenuation of ~ 85-86% in the light beam intensity, due to its high refractive index. For emitted light power higher than 100 mW or incident intensity of ~ 10 mW/mm^2, the intensity was above the activation threshold for up to 5 mm of brain tissue. For a moderate power of 10 mW and incident intensity of ~ 1 mW/mm^2, the intensity was above the threshold for a brain tissue depth of 1.6 mm. The beam with the minimum power emitted modeled assessed here, i.e. 1 mW, did not have sufficient intensity to elicit neuronal activation following transcranial propagation.

The absence of the skull shifted the intensity curves upwards, as expected (Fig. 1g). Craniotomy allowed light beams with moderate initial power of 10 mW to penetrate into depths up to 5 mm. Interestingly, even beams with the minimum emitted power of 1 mW had sufficient intensity for activation at depths of 0.75 mm. A noteworthy observation from this model was that increasing the incident intensity to higher than 1 mW/mm^2 should not have a measurable impact on the activation volume, as the light intensity would be sufficient to trigger neuronal firing throughout the murine brain.

Skull heating during FUS and light exposure was minimal

Convergent FUS and divergent red light exposures were expected to induce a temperature rise on the skull surface. Heating profiles were measured during each exposure *in vivo* with a tissue-implantable

thermocouple. Temperature increased exponentially upon initiation of the FUS exposure and reached a plateau during the 1-min sonication (Fig. 1h). Heating rate and plateau temperature depended on the ultrasonic pulse length. The maximum temperature increase was 0.17ºC, 0.97ºC, and 1.75ºC for pulse lengths of 10 ms, 50 ms, and 100 ms, respectively. A similar trend was observed for light-induced heating, which depended on the light duty cycle. Plateau was reached at a temperature increase of 1.4ºC, 2.4ºC, and 13.1ºC for duty cycles of 5%, 10%, and 50%, respectively. In this study, we used an ultrasonic pulse length of 10 ms and a light duty cycle of 10%. As a result, the maximum temperature increase expected in our experiments were low, on the order of ~ 0.2ºC and ~ 2.5ºC for FUS and light exposure, respectively.

Viral administration does not influence the BBB opening characteristics

Fifty-three male wild-type C57BL/6 mice were used in this study. Most of these animals (n=41) were treated bilaterally and were reserved for the fear-conditioning experiment. These mice were separated into three groups: a) sham (n=11), b) FUS only (n=12), and c) FUS+AAV (n=18). Sham mice were injected with microbubbles but not AAV, and were not exposed to FUS. The remaining mice were treated unilaterally in the left hemisphere, and were used for *in vivo* electrophysiology (n=5), multi-electrode array measurements (n=5), and Ca^{+2} imaging (n=2).

Following FUS treatment, we confirmed BBB opening in the targeted areas with contrast-enhanced T1-weighted MR imaging in 9.4-T magnet. Gadolinium (Omniscan; GE healthcare, Bronx, NY, USA) extravasation, used as a surrogate for BBB opening, was detected throughout the hippocampus, thalamus and amygdala (Fig. 2a). As expected, the ellipsoidal focal volume of the FUS transducer (Fig. 1c) produced a highly localized BBB opening on the transverse plane (diameter ~ 3 mm/spot). In contrast, the BBB opening was widespread along the axial dimension of the FUS beam. The BBB opening volume was measured as 1.15 ± 0.92 mm^3 (n=11), 62.93 ± 7.76 mm^3 (n=12), and 66.18 ± 9.92 mm^3 (n=18), for the sham, FUS only, and FUS+AAV groups, respectively. Contrast enhancement within the exposed brain regions was 3.41 ± 1.14 %, 50.88 ± 4.77 %, and 44.30 ± 8.72 %, respectively. Sham mice did not receive FUS, thus the calculated volume and contrast enhancement were at the noise level. There were no

significant differences for either BBB opening volume or contrast enhancement between the FUS and FUS+AAV groups ($p > 0.05$, Kruskas-Wallis test).

Real-time treatment monitoring confirmed the BBB opening safety

Cavitation activity was passively monitored during FUS treatment (Fig. 2, representative example). We recorded the time-domain signal (Fig. 2c-top), which was then converted to frequency-domain signal (Fig. 2c-bottom) with a fast Fourier transform (FFT). Multiple harmonics were detected during sonication, ranging from the 2nd harmonic (i.e., 3 MHz) to the 6th harmonic (i.e., 9 MHz). Harmonic emissions persisted throughout the 60-s treatment, as confirmed by the corresponding spectrograms (Fig. 2c-right). This was corroborated by the cavitation dose evolution over time (Fig. 2d). Stable cavitation dose rose immediately after microbubbles perfused into the focal volume, in contrast to ultraharmonic and inertial cavitation doses, which remained constant. The harmonic dose decreased slowly over time, due to microbubble clearance from the vasculature (Definity® half-life: 1.3 minutes). The harmonic dose was ~ 50 times higher than both ultraharmonic/inertial doses, establishing that stable cavitation was the dominant cavitation mode during treatment and ensuring the safety of the procedure [27]. The high harmonic-to-inertial dose ratio suggested that the majority of the microbubbles were vibrating in a stable manner, with minimal microbubble collapse and destruction, which could potentially lead to compromised safety of the surrounding vasculature [28]. Cavitation results were corroborated by hematoxylin & eosin (H&E) staining performed 24 h after treatment, showing no red blood cell extravasation or acute FUS-induced trauma (supplementary Fig. 1).

ChrimsonR and cFos are expressed following FUS treatment and light exposure

All treated mice were sacrificed through transcardial perfusion 60 min after excitation with red light (DC: 10%, PRF: 10 Hz, driving current: 500 mA, excitation duration: 300 s), and their brains were processed for histology. Fluorescence microscopy confirmed AAV9 delivery and ChrimsonR expression in the targeted brain regions spanning the entire dorsoventral axis, up to 4.7 mm depth (Fig. 2e and supplementary Fig. 2). ChrimsonR expression was inhomogeneous but mostly restricted within the focal

196 volume (supplementary Fig. 2), and was detectable only in the FUS+AAV group. No tdTomato
197 fluorescence was detected in sham and FUS only groups. Furthermore, there was not tdTomato fluorescence
198 in the contralateral hemisphere of mice treated unilaterally (supplementary Fig. 3). This suggested that the
199 viral vector was not able to cross into the brain parenchyma with an intact BBB. Preliminary experiments
200 with intravenous injection of the AAV9 construct and without FUS exposure did not reveal any tdTomato
201 expression. Therefore, we did not include an AAV only group in our behavioral cohorts to abide by the 3Rs
202 principle, as these were expected to have a similar brain response to sham mice.

203 cFos staining (Cat. # 226017, Synaptic Systems, Göttingen, Germany) was performed to indirectly
204 estimate the incidence and spatial distribution of neuronal activation following red light exposure. Limited
205 cFos was detected in the sham and FUS only groups (Fig. 2e, top and center, representative example). In
206 mice treated with FUS+AAV, we detected extended cFos expression at the vicinity of ChrimsonR-
207 expressing neurons. Increased cFos expression was also detected close to AAV-transfected regions of the
208 thalamus and amygdala, confirming that this activity was indeed light-triggered at depths > 4 mm
209 (supplementary Fig. 4a). cFos was also observed within the cell body of ChrimsonR^{+} neurons
210 (supplementary Fig. 4b).

211

212 ***Red light illumination increased neuronal firing in vivo***

213 Neuronal activation was directly measured in the hippocampus through *in vivo* electrophysiology.
214 ChrimsonR functionality in transduced neurons has been previously established *in vitro* and *in vivo* [24,29].
215 Here, we aimed to confirm that FUS treatment does not compromise the health or functionality of
216 ChrimsonR-expressing neurons. AAV-treated mice were implanted with a 16-channel microdrive with four
217 tetrodes aimed at CA1 neurons (Fig. 3a). Upon light exposure, we detected multiple action potentials from
218 all electrodes, which were later sorted with a spike sorting software. The action potentials from individual
219 neurons had similar waveforms and latencies across channels (Fig. 3b) and across cells (supplementary Fig.
220 5).

Firing rates were calculated at baseline and during illumination. We used both a red LED (λ = 635 nm) and a blue LED (λ = 470 nm) at equivalent light intensities, to record light-induced action potentials (Fig. 3c). Blue light served as a control, to measure potential electronic noise from the LED driver, wiring, etc. Other sources of noise, such as the photoelectric and Seebeck effects (supplementary Fig. 6) were excluded due to the material of the tetrodes (90% Pt/10% Ir). Firing rates in baseline and during blue-light exposure were similar, estimated at 0.99 ± 1.88 and 0.85 ± 1.69 spikes/second, respectively ($p = 0.91$, two-sample t-test). In contrast, red-light exposure increased the firing rate to 4.78 ± 2.21 spikes/second, significantly higher than both baseline ($p = 0.03$) and blue light ($p = 0.02$).

The influence of red light parameters on the firing rate was examined in separate experiments by changing the LED driving current (i.e., the optical power and light intensity at the air/brain interface), the pulse repetition frequency, and the depth of recording (Fig. 3d and supplementary Fig. 7). The firing rate increased from baseline up to a driving current of 10 mA (optical power: 1.24 mW), but then plateaued for currents higher than 50 mA (6.8mW or ~ 0.1 mW/mm^2 at 3 mm distance from the source). This was in good agreement with our light propagation model (Fig. 1g), which predicted that the intensity would be above the activation threshold at a recording depth of 2 mm and an optical power between 1 mW and 10 mW. Higher optical power was not expected to trigger more neuronal activation, which was confirmed here (Fig. 3d-left). Furthermore, increasing the pulse repetition frequency increased the firing rate (Fig. 3d-right). The increase was mostly noted between 1 Hz and 10 Hz (~ 2 orders of magnitude). The rate of increase was reduced for frequencies higher than 10 Hz, with a 1.3× increase between 50 Hz and 100 Hz.

Ca^{2+} concentration increases in dissociated ChrimsonR$^+$ neurons during illumination

Neuronal activation was visualized with Ca^{2+} imaging of ChrimsonR-expressing dissociated neurons. The purpose of the experiment was to confirm that genetically modified neurons exposed to FUS are viable and able to respond to external stimuli (i.e., red light and KCL infusion). ChrimsonR expression was confirmed through fluorescent imaging of the tdTomato-fluorescent neurons. Cell cultures with the

highest number of ChrimsonR$^+$ neurons were imaged in an inverted microscope by 340 nm and 380 nm excitation light to measure the ratiometric Fura-2 signal, which was indicative of the intracellular Ca^{2+} concentration. Cell health was assessed by direct infusion of a 150 mM KCl solution. Cells expressing ChrimsonR were manually selected and analyzed independently. We did not analyze cells that had no detectable ChrimsonR. Cells exposed to red light had increased intracellular Ca^{2+} concentration during illumination, which was indicative of cell activation (Fig. 3e). Despite the lack of spectral overlap, there was a notable increase of the background intensity. We detected a sustained amplitude of Ca^{2+} signal throughout light exposure (Fig. 3f), which was lower than the positive control experiment with KCl infusion (supplementary Fig. 8), as expected.

Remote light activation influences the spatial distribution of neuronal activity

The spatial distribution of cortical activation was mapped through multi-electrode array (MEA; Neurogrid) measurements (Fig. 3g). Using contrast-enhanced MRI as a guide, we placed the MEA on the cortical area corresponding to the BBB opening vertical column. We chose mice with high level of cortical BBB opening, used a surrogate for potential cortical ChrimsonR expression. Prior to MEA placement, anesthetized mice underwent craniotomy to enhance the signal-to-noise ratio of the recorded signals. Sporadic firing was recorded when light was off (Fig. 3g-top). Turning the LED on triggered substantial activity recorded by most surface electrodes (Fig. 3g-bottom). Integrating the power of the time-domain signal over time revealed the average power per electrode. A map of the detected power showed the spatial distribution of cortical activation (Fig. 3h). The center of the BBB opening had lower power than the outskirts of the opening area, suggesting that power modulation was specific to the intervention. Spectral analysis of the time-domain signals revealed an overall power increase following light excitation (Fig. 3i). The wideband increase suggested a larger and more frequently occurring electrical activity during the “light on” state. However, the spectral power difference was considerably higher during illumination for frequencies lower than 20 Hz (Fig. 3i and supplementary Fig. 9a-b). This observation was evident in the temporally-resolved spectrograms (Fig. 3j and supplementary Fig. 9c-d), where illumination triggered a

wideband increase in the detected cortical power (supplementary Fig. 9e), which was dominant at low frequencies.

FUS treatment and ChrimsonR activation influence the long-term fear perception

Our remote optogenetics method has the advantage of activating multiple areas simultaneously. Here, we treated and activated multiple brain regions, such as the hippocampus, the thalamus, and the amygdala (Fig. 2a), all within the focal volume of our FUS transducer. These areas are part of the brain network affecting fear perception and expression. We hypothesized that the FUS treatment and red light exposure would affect the freezing behavior in a fear-conditioning test. To that end, mice underwent a 3-day long behavioral assessment, which was recorded with a camera. Behavioral testing was conducted at least 3 months after FUS treatment, to eliminate any short- or mid-term compounding effects from the homeostasis alteration induced by this intervention. During habituation (day 1), mice were placed for 3 minutes on the conducting grid within a transparent cylinder (Fig. 4a). The 16-cm-high cylinder was fixed at the center of an isolated chamber. During conditioning (day 2), mice were exposed to red light continuously (DC: 10%, PRF: 10 Hz, driving current: 1,000 mA, excitation duration: 390 s) and were presented with 3 tones. Due to the distance between the light and the mouse head (~ 130 – 150 mm), the light intensity was expected to be above the activation threshold at depths up to 2 mm (supplementary Fig. 10). Each tone was followed by a 2-s electric shock. During recall (day 3), mice were presented with 3 tones, which were not followed by a shock. We hypothesized that mice would progressively freeze more on day 2, and less on day 3, assuming their working memory dictated there was no shock coming during recall.

All mice roamed around the chamber without considerable freezing during habituation (Fig. 4b). The average freezing score per second was ~ 0 for the entire 3-min session and for all groups tested (0: motion, 1: freezing). In contrast, mice progressively froze more in conditioning following the first electric shock. Each subsequent shock caused longer freezing time. Mice from all cohorts froze up to 60% of the time towards the end of the conditioning trial. In the beginning of the session on day 3, all subjects froze

considerably more than the respective period on days 1 and 2. However, sham mice froze on average more than the FUS treated mice (both FUS only and FUS+AAV groups). This behavior was evident throughout the recall trial. During the 60-s-long first tone, all mice increased their freezing time. Freezing behavior following each tone was distinct for each group, with FUS+AAV mice freezing progressively less over time, in contrast to sham and FUS only mice, which had similar responses over time.

We then focused on the startling response during each tone (Fig. 4c and 4d). The average freezing time (i.e., time of no motion divided by the duration of each tone) increased for all groups in the conditioning session (Fig. 4c). FUS-treated mice had a moderately lower freezing time during tone 2 ($p = 0.02$, Kruskas-Wallis test), but this difference was no longer seen in tone 3 ($p = 0.41$). Freezing behavior was significantly different in FUS-treated mice compared to sham mice on day 3. Sham mice froze ~ 80% of the time during each tone throughout the recall session. FUS-treated mice had a significantly lower freezing time than sham mice in every tone ($p = 0.036$ in tone 1, $p = 0.03$ in tone 2, and $p = 0.032$ in tone 3). Mice treated with FUS+AAV froze 10% less with each tone (slope: -10.94, linear regression), in contrast to sham and FUS only mice which did not change their average freezing time for each tone (slopes: -0.23 and -0.57, respectively). The FUS+AAV freezing time slope was significantly different than the sham slope ($p = 0.05$). In contrast, the FUS only slope was not different compared to the sham slope ($p = 0.94$). The slope difference between FUS and FUS+AAV was notable, but not statistically significant ($p = 0.11$). Although this is a preliminary sign of enhanced working memory in the FUS+AAV mice, likely due to light-induced network activation in the hippocampal region (depth < 2 mm, supplementary Fig. 10), the effect was minimal. Post-hoc analysis of individual groups showed that both FUS only and FUS+AAV groups had a significantly lower freezing time in tone 1 of recall (Fig. 4d), indicating the FUS treatment itself induced a long-term modulation of fear recall. However, only FUS+AAV mice froze significantly less in tones 2 and 3 than sham mice (Fig. 4d), suggesting that light-triggered neuronal activation might influence the dynamic adaptation to the change of a fearful memory valence.

Discussion

In this work, we introduced a method for non-invasive optogenetics to remotely and selectively excite defined brain regions through the intact skull with a mm spatial and ms temporal precision. We showed that FUS-mediated delivery of the AAV-encoded red-shifted opsin Chrimson [24], in combination with transcranial red light exposure elicit neuronal activation, confirmed through cFos expression (Fig. 2) and a battery of electrophysiology measurements (Fig. 3). Furthermore, we showed that fear response can be modulated months after the FUS treatment following illumination of light-sensitive networks (Fig. 4).

Red-shifted channelrhodopsins have become essential in applications requiring multimodal excitation/inhibition without crosstalk [24] or activation of deep structures [17]. The ChrimsonR channel was delivered deep into the brain in this study (Fig. 2e and supplementary Fig. 3) and red light exposure caused activation - assessed through cFos staining - at depths up to 4 mm (Fig. 2e and supplementary Fig. 4). This was expected from modeling which showed that at the emitted optical powers used here (> 100 mW), the light intensity would be above the activation threshold across the entire murine brain depth (Fig. 1g). cFos staining was performed in mice which were exposed to light with a minimal distance between the LED and their head (~ 3-5mm). However, the behavioral experiment was performed in a setup where the light source was remote and distant (Fig. 4a). Based on the model predictions, light intensity greatly decreased over the 130 – 150 mm path from the LED to the behaving mouse head (supplementary Fig. 10). We deduce that hippocampal neurons were likely activated during light stimulation (activation depth < 2 mm), potentially improving the working memory of AAV-treated mice (Fig. 4c). Sensory input processing and fear recall recruits multiple brain regions, which have been previously characterized through invasive optogenetic methods [13,14]. Compared to similar optogenetic studies, the behavioral effects observed here were small, potentially due to the lack of special specificity in our FUS setup and the amount of transcranial light intensity.

MEA measurements suggested a power modulation specific to the FUS-treated area during light exposure (Fig. 3h). It is likely that the treated region had a lower activity due to excessive opsin expression or FUS-induced micro-scarring at the center of the focus. We speculate that brain-wide networks controlling

locomotor or somatosensory activity may be influenced by this stimulation. Interestingly, the spectral content of neuronal firing (Fig. 2i-j and supplementary Fig. 9) was consistent with previous work on ChrimsonR, which showed that spiking probability greatly reduced for excitation frequencies higher than 20 Hz [24]. Further work should focus on transducing either excitatory or inhibitory neurons along the fear network non-invasively, and also performing alternative behavioral tests, e.g. the Morris water maze test, for spatial working memory assessment.

FUS has been previously used both to deliver genes of interest [21,30] and to selectively excite mechanosensitive ion channels [3,4,31]. An exciting neuroengineering approach that benefits from FUS-mediated viral delivery is acoustically-targeted chemogenetics (ATAC) [32,33]. ATAC combines the spatial selectivity of FUS therapies with chemically-activated receptors (i.e., DREADDs), providing a scalable method of controlling specified networks through intravenous CNO administration. The authors showed that, similarly to this study (Fig. 4), CNO-treated mice had lower freezing time in a fear conditioning test, compared to saline-treated controls [32]. Despite its scalability, ATAC has limited temporal control over the stimulation duration, which depends on the circulation time of CNO. Ultrasound has also been used as a thermal stimulus following direct injection of lentivirus-encoded thermally-sensitive TRPV1 ion channels in sonothermogenetics [34]. Sonothermogenetic activation evoked locomotor behavior in freely moving mice, only when local temperature during high-duty-cycle sonication exceeded 42^{o}C. However, this approach required either anesthesia or implantation of a construct bearing the FUS transducer onto the mouse skull, hindering application in larger species or humans. Furthermore, activation is constrained within the focal area of the transducer which has to be physically coupled with the head, so only a defined brain region can be currently activated at a time. To our knowledge, this is a unique approach that combines mm spatial precision across multiple brain compartments, ms temporal resolution, non-invasiveness, remote activation, and scalability to larger species, including humans.

In this study, we chose an AAV9 serotype encompassing the synapsin promoter for selective transgene expression in the targeted area (Fig. 2e). This choice was based on previous studies which found that intravenous injection of AAV9 leads to limited region-dependent neuronal transduction without FUS

[35], and to widespread transduction when coupled with FUS treatment [36]. Efficient viral delivery was achieved here by using relatively high acoustic pressures (i.e., 0.8 MPa) which instigated strong harmonic emissions (Fig. 2c and 2d), leading to a substantial BBB opening (Fig. 2a). In this study, we did not detect neuronal transfection without BBB opening. To facilitate viral transduction and gene expression, new generations of AAV serotypes are being designed, in an effort to enhance FUS-mediated delivery across the BBB and neuronal tropism, while limiting non-specific transduction [37]. Out of the natural AAV serotypes, AAV6 has been shown to result in lower liver biodistribution compared to a mosaic AAV1&2 and AAV9 vectors following intravenous administration [38]. A limited number of studies have established viral transduction in larger animal models, like non-human primates (NHPs), using capsid mutants such as AAV-PHP.B [39]. However, these were achieved with intra-arterial or intrathecal injection of the viral particles. Similar viral vectors with chimeric capsids able to cross the BBB (e.g., AAV-PHP.eB and AAV-PHP.S [40,41]) have been recently used for performing deep optogenetics without intracranial surgery [20]. While AAV-PHP vectors can be adapted to transduce specific neuronal types (e.g., raphe nuclei or Purkinje neurons [20]), our non-invasive optogenetics method permits increased spatial control of opsin delivery within complex neuronal circuits and neuronal types. Furthermore, our approach allows non-invasive and localized delivery of any viral or non-viral gene delivery platform into the brain. FUS-mediated gene delivery may facilitate other non-invasive optogenetics approaches, such as the use of circulating mechanoluminescent nanoparticles to produce blue light within the vasculature [23]. In future work, we will attempt intravenous administration of viral vectors in NHPs, to test the reproducibility of the results shown here in larger species.

The proposed method, as applied here, has a number of limitations. First, red light ($\lambda \sim 620 – 700$ nm) may be appropriate for transcranial stimulation in the rodent brain, but it is unlikely to penetrate through the thicker and more inhomogeneous primate skull. We have not performed measurements or simulations with a human skull, but it is expected that the attenuation will be significantly higher and only superficial cortical regions might be accessible for stimulation. Opsins that are sensitive to longer wavelength light (e.g. near infrared) have been recently engineered [42,43], and could be potentially used for non-invasive

excitation in NHPs and humans. Alternatively, upconversion approaches could be employed to convert infrared to visible light in deep brain regions [19]. However, this would entail an additional nanoparticle delivery session prior to each excitation, which could be performed using the same FUS-based approach [44,45].

Second, our FUS system had a defined focal volume with an ellipsoidal shape (i.e., 7.5 × 1 × 1 mm^3) and allowed limited control of viral delivery across the axial dimension (Fig. 1c). This characteristic was used to deliver AAV particles across multiple fear-related regions, but it is likely that improved spatial control will benefit the study of more complex networks, such as the nigrostriatal pathway in Parkinson's disease [46]. The behavioral outcome of activating multiple brain regions at once is difficult to control and interpret. Future improvements include the design of transducers with smaller focal volumes (e.g., transducers with lower F-number) or the use of acoustic holography to bend the acoustic focus into arbitrary brain volumes [47–49], in order to express ion channels within precisely targeted regions. Electronic steering from multi-element ultrasound arrays may also allow BBB opening and viral delivery at multiple spots [50]. To improve the inhomogeneous viral delivery and ChrimsonR expression, we aim to apply rapid short-pulse (i.e., μs pulse length) sequences, which produce more homogeneous cavitation activity [51,52] and BBB opening [53] than those with long-pulse (i.e., ms pulse length) sequences.

Third, to avoid implantation of LED sources onto the mouse skull during behavioral evaluation, we chose to place the LED light at a height of 160 mm. This was necessary to uniformly cover the movement area of the fear conditioning chamber and avoid physical contact with the animal itself. However, the light intensity reaching the mouse head was greatly reduced, and was likely not sufficient to excite deep-seated transfected neurons. Nevertheless, based on modeling findings, we expected light intensity above the activation threshold in the hippocampal area (Supplementary Fig. 10). Future improvements may thus include using lighter LED sources or performing behavioral tests that do not require animal motion (e.g., grasp test). Additionally, we have not investigated ChrimsonR expression in peripheral neurons. Given that the whole body was exposed to light in the behavioral experiment, it is likely that peripheral activation might have occurred. Peripheral gene expression will be assessed in our future work.

Finally, FUS treatment itself may elicit downstream effects that are potentially long-lasting [54], for example neurogenesis [55–57], angiogenesis [58], functional connectivity modulation [59], or micro-scar formation [60]. This was evident in our behavioral findings, where mice treated only with FUS presented a notably different freezing behavior compared to sham mice (Fig. 4). The pressures used here were relatively high to allow higher AAV dose into the brain. However, a safer FUS application by using lower pressures and higher duty cycle will also be employed in the future [46]. The influence of each of these downstream effects on behavioral outcomes, along with their dependence on the acoustic parameters used for gene delivery, will be investigated in future studies. Nevertheless, the non-invasive optogenetics method has the potential to improve and expand the way normal and pathological brain function is studied and controlled. The proposed non-invasive optogenetics method can be applied in several neuroscience studies, to further elucidate brain-wide circuits responsible for functions such as perception [10], memory retrieval [11], emotional valence [12], or fear recall [13,14]. It can also be used as a treatment method for pathological conditions, such as epilepsy or coma. Finally, it can be applied in combination with other genes that are proposed for gene therapy in neurodegenerative diseases, but also in other organs such as the eye and the heart.

Methods

FUS transducer and LED calibration

Prior to the experiments, the FUS transducer and LED were calibrated using a hydrophone and an optical sensor, respectively. Ultrasound calibration was conducted in a tank filled with deionized and degassed water. The FUS transducer (center frequency: 1.5 MHz, focal depth: 60mm, radius: 30mm; nominal axial full-width half-maximum (FWHM): 7.5 mm, nominal lateral FWHM: 1 mm; Imasonic, France) was mounted on a 3D positioning system (Velmex Inc., Lachine, QC, Canada) and submerged into the water. A function generator (33500B series; Agilent, Palo Alto, CA, USA) was used to drive the FUS transducer (center frequency: 1.5 MHz, focal length: 60 mm, diameter: 60 mm; Imasonic, France) through a 50-dB power amplifier (325LA, 25 Hz, 50dB gain; E&I, Rochester, NY, USA). The same configuration was used for *in vivo* experiments. A capsule hydrophone (HGL-0200, -3-dB frequency range: 0.25-40 MHz, electrode aperture: 200 μm; Onda Corporation, Sunnyvale, CA, USA) was fixed below the transducer and captured the emitted pressure waves. We performed a raster scan with an in-plane resolution of 100 μm and axial resolution of 200 μm, in order to determine the axial and lateral beam profiles. The pressure-voltage relationship was determined by varying the applied voltage and measuring the emitted pressure at the center of the acoustic focus. Ultrasound attenuation due to the murine skull was assumed to be 18% at 1.5 MHz, based on previous work [61].

The 635-nm LED (LED635L, power dissipation: 500 mW, DC forward current: 500 mA, center wavelength: 635 nm, FWHM: 15 nm, half viewing angle: 7°, optical power at 250mA: 170 mW; Thorlabs, Newton, NJ) was calibrated in air using a S120VC photodiode power sensor (sensitivity range: 200-1100 nm, power: 50mW; Thorlabs) connected to a PM100A digital photometer (Thorlabs). The sensor was attached to the 3D positioning system (Velmex Inc.) and was automatically translated along all three axes to acquire the 3D beam profile. The scan step size was 1 mm, and the axial, lateral, and elevational ranges were 30 mm, 20 mm, and 20 mm, respectively. The LED was driven by a high-power DC2100 LED driver (Thorlabs) at different currents (range 1 – 500 mA) to determine the optical power (in mW) and irradiance or intensity (in mW/mm^2) at variable depths. Finally, an *ex vivo* murine skull and a murine brain were positioned between the LED and the optical sensor to measure the transmission coefficient through skull and brain tissue, respectively.

Heating profiles were measured with a tissue-implantable thermocouple microprobe (IT-23, type T; Physitemp Instruments, Clifton, NJ, USA). The thermocouple was placed at the skull site of entry for both the FUS

and light beams. Temperature was continuously recorded at 100 Hz using a purpose-built function in MATLAB (MathWorks, Natick, MA, USA), and was later re-sampled to 1 Hz. For the light exposure, the sampling frequency was 0.2 Hz. We measured the FUS-induced skull heating at different pulse lengths (i.e., 10 ms, 50 ms, and 100 ms), keeping all other sonication parameters constant. Similarly, we measured light-induced skull heating at different optical duty cycles (i.e., 5%, 10%, and 20%). FUS heating profile was measured during FUS only experiments, with the thermocouple fixed onto the skull and below the coupling water container. For these experiments, the center of the focal volume was placed 3 mm below the skull surface. Light heating profile was measured with the LED source at a distance of ~ 10 mm from the skull, to imitate the light exposure conditions prior to sacrifice. Note that for behavioral experiments, skull heating was expected to be drastically lower, due to the increased distance between the skull and the light source (130 – 150 mm).

Light propagation model

Using the transmission coefficients determined experimentally, we applied an analytical light propagation model to estimate the light intensity across different depths of the mouse brain. We followed an approach described before by Aravanis et al. [15]. The model comprised of three compartments: air, skull, and brain tissue. Each compartment had specified refractive index n, angle of beam divergence θ, and transmission coefficient T. The aim was to estimate the light intensity I at a tissue depth z.

First, we calculated the scattering coefficient per unit thickness $S_i = (1-T_i)/z_i T_i$, where T_i was the transmission coefficient of each compartment, z_i was its thickness, and $i = 1, 2, 3$ corresponded to air, skull, and brain, respectively. The fractional intensity decrease due to conical geometry was estimated as $\rho_i = r\sqrt{(n_i / NA)^2 - 1}$, where r was the radius of the LED and NA its numerical aperture. The angle of beam divergence was calculated as $\theta_{div,i} = \sin^{-1}(NA/n_i)$. Finally, the intensity profile was approximated as $I(z) = I_0 \prod_{i=1}^{3} \rho_i^2 / \left[(S_i z_i + 1)(z_i + \rho_i)^2 \right]$. This model assumed a uniform and isotropic transmission coefficient throughout the skull and brain, ignoring local inhomogeneities, e.g. myelination. The activation threshold for the ChrimsonR channel was assumed to be ~ 0.03 mW/mm^2, based on previous studies [18,24].

Animals

All *in vivo* experiments were approved by the Institutional Animal Care and Use Committee (IACUC) of Columbia University (protocol # AC-AABG4559) and were carried out in accordance with relevant guidelines and regulations of the National Institutes of Health. A total of 53 male wild-type C57BL/6 mice (mass: 22 ± 4 g, age: 2–3 months at the time of FUS treatment) were used for the *in vivo* experiments. Mice were exposed to a 12 h light/dark cycle and had access to chow and water *ad libitum*. We used a separate mouse cohort for *in vivo* electrophysiology (n=5), multi-electrode array measurements (n=5), and Ca^{2+} imaging (n=2). These mice were treated unilaterally in the left hemisphere, targeting the hippocampal area. The mice reserved for the behavioral experiment were randomly allocated into three experimental groups: sham (n=11), FUS only (n=12), and FUS+AAV (n=18). These mice were treated bilaterally, in multiple brain regions, i.e. amygdala, thalamus, and hippocampus, due to the size of the focal volume (7.5 mm × 1 mm).

Ultrasound treatment

FUS experiments in mice were conducted following a procedure described earlier.[62,63] Briefly, mice were anesthetized with inhalable isoflurane delivered through a digital anesthesia system (SomnoSuite; Kent Scientific, Torrington, CT, USA). Isoflurane was mixed with oxygen at 2-3% for induction and 1.2-1.5% for maintenance of anesthesia. Anesthesia depth was assessed with a toe pinch on regular intervals (3 – 5 min). The animals' head was fixed within a stereotaxic frame (Kopf Instruments, Tujunga, CA, USA) and their fur was shaved with clippers. Remaining hair was removed with a depilatory cream, applied for less than 30 seconds. Targeting was achieved by placing a metallic grid on the lambdoid suture and then performing a raster scan with the passive cavitation detector operating in pulse-echo mode, as described earlier [61,64].

The focal volume was placed in the hippocampal area of the left hemisphere (+2 mm ventral, -2 mm lateral, starting from lambda). Given the measured size of the focus (1 mm × 1 mm × 7.5 mm), BBB opening and viral delivery were expected throughout the axial depth of the targeted transverse region, spanning areas including the motor/somatosensory cortex, hippocampus, thalamus, and amygdala. Once targeting was completed, a control sonication was performed prior to microbubble administration, to acquire a baseline signal. Definity® microbubbles (0.5 µl/g; Lantheus, Billerica, MA, USA) were then administered as a bolus through a tail vein catheter. At the same time, the therapeutic sequence (center frequency: 1.5 MHz, peak-negative pressure: 800 kPa, pulse length: 1 ms or

1,500 cycles, pulse repetition frequency: 5 Hz, pulse number: 600) was initiated through a customized Graphics User Interface in MATLAB. The total treatment time was 2 min. The pressure was chosen based on previous studies showing efficient delivery of viral vectors or compounds with molecular weight on the order of MDa [65,66]. For the behavioral cohort, each hemisphere was treated for 1 min. The transducer was moved to the contralateral hemisphere by translating the 3D system by 4 mm along the lateral dimension. We randomly started treatment from the left or right hemisphere, to minimize the bias of enhanced BBB opening in either hemisphere due to higher microbubble concentration in the beginning of the FUS treatment.

The viral vector used in this study had an AAV9 serotype. Specifically, an AAV9.Syn.ChrimsonR-tdTomato.WPRE.bGH vector was purchased from Addgene (# 59171-AAV9, titer: $\geq 10^{13}$ vg/ml). This vector (size: 6,864 bp) was pioneered by Klapoetke et al. [24], and encompasses a synapsin promoter for neuron specificity [67], a tdTomato fluorescent reporter for expression detection (C terminal), and the ChrimsonR channel, which is a red-shifted channelrhodopsin variant. Chrimson has fast kinetics, with a time to peak of ~ 7 ms and a τ_{off} of ~ 20 ms [24]. In this study, we chose an on-time of 10 ms and an off-time of 90 ms, to allow for complete activation and recovery of the light-gated ion channel, respectively. AAV particles were stored at -80°C and were thawed before injection. We intravenously injected a total of 1.67×10^{11} vg/mouse, mixed with the Definity® microbubbles.

To confirm the location and spatial extent of BBB opening, we injected 0.2 ml of gadolinium (Gd)-based contrast agent (Omniscan; GE healthcare, Bronx, NY, USA) in the peritoneal cavity after FUS treatment. Mice were fixed within a 3-cm birdcage coil and scanned with a 9.4-T MRI system (Bruker, Billerica, MA, USA). We acquired contrast-enhanced T1-weighted 2D FLASH scans (TR: 230 ms, TE: 3.3 ms, flip angle: 70°, number of excitations: 18, pixel size: 85 μm × 85 μm, slice thickness: 500 μm, receiver bandwidth: 50 kHz).

The acquired scans were loaded onto MATLAB for processing and quantification. We analyzed the axial slices of each mouse brain. First, a region of interest was defined in a brain area without contrast enhancement, to measure the baseline signal intensity. Then, an ROI covering the entire brain was drawn in each axial slice. We counted pixels with an intensity higher than the mean baseline intensity plus 3 standard deviations. The sum of pixels in each slice provided the BBB opening area per slice. The BBB opening volume was calculated as the product of the total area across all slices (n = 20) by the slice thickness (i.e., 500 μm). Additionally, we calculated the % contrast enhancement by dividing the mean difference between BBB opening areas and baseline over the mean baseline intensity.

Real-time acoustic monitoring

Microbubble emissions were monitored in real-time through a passive cavitation detector (V320-SU, center frequency: 7.5 MHz, diameter: 10 mm; Olympus, Waltham, MA, USA) and saved to a PC for off-line processing in MATLAB. Cavitation signals were amplified with a pulser-receiver (Part No. 5072; Olympus Industrial) and then recorded using a GaGe oscilloscope card (Part No. CSE1422, 14 bit; Dynamic Signals LLC, Lockport, IL, USA). The time-domain signal (114,688 time points at a sampling frequency of 100 MSa/s) was analyzed in accordance to previous work.[26,62] First, a fast Fourier Transform (FFT) was performed to derive the spectral content of the microbubble response for each pulse (FFT points: 114,688). Second, we filtered three spectral areas of the signal, namely the harmonic, ultraharmonic, and broadband regions.[57] Harmonic and ultraharmonic regions were defined within a 10 kHz spectral window around the harmonic (i.e., $f_h = nf_0$) and ultraharmonic (i.e., $f_u = (n+1) f_0 / 2$), for n = 1,2,…, 6. The broadband or inharmonic regions were defined within these windows, i.e. $f_{h,n} + 10kHz < f_b < f_{u,n} - 10kHz$ and $f_{u,n} + 10kHz < f_b < f_{h,n+1} - 10kHz$. Cavitation doses were calculated as the root-mean-square (RMS) of the spectral amplitude within each domain, i.e. $dSCD_h = \sqrt{\left\langle |FFT|^2_{f_{h,n}} \right\rangle_n}$, $dSCD_u = \sqrt{\left\langle |FFT|^2_{f_{u,n}} \right\rangle_n}$, and $dICD = \sqrt{\left\langle |FFT|^2_{f_b} \right\rangle}$.

Light exposure

Transcranial light exposure was conducted using the 635-nm LED positioned at variable distance from the murine head. For anesthetized mice, the distance was ~ 10 mm. For freely behaving mice in the fear conditioning test, the distance was ~ 130-150 mm. The LED was driven by the DC2100 LED driver at 10% duty cycle (DC), 1-10 Hz pulse repetition frequency, forward current 1- 500 mA, and irradiance of 0.08 – 40 mW/mm^2. Most exposures were conducted at 10% DC, 10 Hz PRF, 500 mA, and 40 mW/mm^2, unless otherwise stated. The total light exposure duration prior to euthanasia was 5 min, while the total duration for the behavioral experiment was 6.5 min (equal to the session duration on conditioning day). Mice were sacrificed approximately 60 min after light exposure, to allow for sufficient expression of cFos in the excited neuronal bodies.

Immunohistochemistry

Animals were first deeply anesthetized and then transcardially perfused with 30 ml of PBS, followed by 60 ml of 4% paraformaldehyde. Brains were extracted and immersed in PFA for at least 24 h followed by sucrose for 48 h. The brain samples were then frozen on dry ice, prior sectioning with a cryostat into 35 μm coronal sections. Floating sections were collected for immunohistochemistry. Sections were first washed with PBS 3 times, and then incubated in a 0.5% Triton-X-100 with 5% normal donkey serum (NDS), diluted in 1× PBS. The samples were then incubated on a shaker with rat anti-cFos antibody (1:500, Cat. # 226017; clone 108B5H5; Synaptic Systems, Göttingen, Germany), 5% NDS, and 0.2% Triton-X-100, for 24 h at 4°C. On day 2, the sections were washed with PBS 3 times, incubated on a shaker with the secondary donkey anti-rat Alexa Fluor 488 antibody (1:1000, Cat. # A21208, highly crossed-absorbed), 5% NDS, and 0.2% Triton-X-100, for 60 minutes at room temperature. The sections were then rinsed 3 times for 10 min in 1× PBS, and transferred to DAPI solution (1:1000 DAPI work solution) for 5 min on a shaker and at room temperature. Finally, sections were rinsed 3 times for 5 min in 1× PBS, and then mounted on a slide and cover slipped with fluoromount (Cat. # F4680-25MM; Sigma Aldrich, St Louis, MO). Stained slices were imaged with a fluorescence microscope (Leica DM6) at 10x and 20x in the red (tdTomato - ChrimsonR), green (Alexa Fluor 488 – cFos), and blue (DAPI) channels. For cFos imaging, we focused on areas with high tdTomato signal, indicative of AAV9 delivery and ChrimsonR expression. Similar areas were imaged for the sham and FUS-only groups, to allow for a comparison of neuronal expression across groups.

***In vivo* electrophysiology**

AAV9-treated mice reserved for *in vivo* electrophysiology were implanted with a 16-channel stainless steel microdrive (Axona Ltd., UK) fitted with 4 tetrodes (90% Platinum - 10% Iridium, California Fine Wire Co., CA, USA) for recording neural activity. Mice were first anesthetized with a mixture of ketamine/xylazine (100 mg/ml and 15 mg/ml, respectively) prior to surgical implantation. A bur hole was opened in the skull above the hippocampus (AP – 3mm, ML – 2mm, DV + 1.5 mm), and jeweler's screws were inserted into the skull to secure the implant. One screw was connected with a wire, which served as a reference electrode. A transparent sealant (Kwik-Sil; World Precision Instruments, Sarasota, FL, USA) was used instead of dental cement, to permit red light penetration into the brain. Mice were allowed to recover for at least a week after surgery, before undergoing optogenetic excitation.

During the recording sessions, mice were anesthetized with a mixture of oxygen and 1-3% isoflurane, and were fixed within a stereotaxic apparatus. A Faraday cage was placed around the recording setup, to reduce electronic noise from the environment. The recording tetrodes (25μm, 90% Pt/10% Ir) were inserted into the microdrive, and were connected to an electrophysiology setup (Axona, St. Albans, UK).[68] Distinct neurons were separated based on their spike-firing rate, amplitude, waveform and refractory periods using the spike sorting software Tint (Axona). Changes in neuronal firing were visualized with the SigTOOL interface in Matlab.[69] We measured the firing rate while varying the forward current (1-500 mA), the PRF (1 – 100 Hz), the light wavelength (red-635nm vs. blue-470nm), and the depth of recording (1 – 2 mm). A series of control recordings were performed with the LED light and the electrodes alone (without the presence of a mouse), to ensure the lack of optically-induced or circuit-induced noise.

Ca^{2+} imaging

We followed a modified protocol described in Kuehl-Kovarik et al,[70] to perform acute dissociation of AAV-transfected neurons prior to Ca^{2+} imaging. Briefly, two C57BL/6 male mice (age: 2 months, mass: 20-22 g) were used for the experiments. The mice were anesthetized with isoflurane, and then decapitated. The brain was rapidly removed and placed in ice cold oxygenated low-calcium artificial cerebral spinal fluid (ACSF; in mM: 108 NaCl, 3.5 Cl, 0.7 $MgSO_4$, 26 $NaHCO_3$, 1.7 NaH_2PO_4, 9.5 Na gluconate, 5.5 Glucose, 7.5 sucrose, 0.1 $CaCl_2$). The brain was trimmed and the AAV9-transfected region, which was selected based on T_1-weighted MRI scans of the treated mice, was kept intact for slicing. Parasagittal slices (thickness: 500 μm) were cut with a Leica VT1200 S vibratome and maintained in A-CSF (aerated with 95% O_2, 5% CO_2) at 30ºC for 60 min prior to dissociation. Slices were placed in proteinase K (Sigma, 0.2 mg/ml) in PIPES buffer (in mM: 115 NaCl, 5 KCl, 20 PIPES free acid, 1 $CaCl_2$, 4 $MgCl_2$, 25 dextrose, pH 7.0; aerated with 100% O_2) at 30 °C for 5 min, rinsed in PIPES buffer, and placed in trypsin (Sigma Type XI; 1 mg/ml) in PIPES buffer at 30 °C for 35 min. Slices were rinsed 4–5 times in PIPES buffer, and neurons were isolated by trituration with flame-polished Pasteur pipettes in ice cold PIPES buffer containing 0.1% DNase. The resulting solution was diluted 1:2 with Neurobasal-A/B-27 (10888-022, A14097, Gibco, 50:1). Cells were plated on laminin (L2020, Sigma, 25 μg/ml in HBSS, 14170161, Gibco) pre-coated glass culture dishes, incubated at 37°C (5% CO_2) for 20–30 min to allow adherence, rinsed, and covered with Neurobasal A/B-27 to which 5 ng/ml β-FGF (Sigma, SRP4038) and 1.0 mM APV (Sigma, A5282) was included. Neurons were incubated for 17–24 h prior to Ca^{2+} imaging.

Following a day of incubation, cultured neurons were imaged in a fluorescence microscope to confirm ChrimsonR expression. We selected the culture dishes containing cells with the strongest ChrimsonR fluorescence signal and transferred them to an Olympus inverted microscope (IX81) for Ca^{2+} imaging. The extracellular recording solution contained (in mM) 145 NaCl, 5 KCl, 10 Hepes, 10 Glucose, 2 CaCl2, MgCl2, adjusted to 325 mOsm with Sucrose and pH 7.3 with NaOH. The LED light was fixed at a distance ~ 20 mm at an angle of 45^{o} compared to the imaging plane. Ratiometric dye Fura-2 was introduced into the neuronal cultures by incubating the cells with Fura-2 (Thermo Fisher Scientific, 5 μM) and Pluronic F-127 (Thermo Fisher Scientific, 0.1%) for 30 min. Fura-2AM crosses cell membranes and once inside the cell, acetoxymethyl groups are removed by cellular esterases. Removal of the acetoxymethyl esters regenerates Fura-2 inside the cells. Following washout of the unbound Fura-2 AM, Fura-2 fluorescence was excited by two wavelengths, 340nm and 380 nm, respectively, as the ratio of the fluorescence emission by these two excitation wavelengths correlates with the cytosolic free calcium concentration. Time-lapse images were collected at 0.5 fps frame rate and analyzed using MetaFluor 7.5.6.0 (Molecular devices, San Jose, CA, USA). Videos were recorded without and with red light illumination at a 40x magnification. At the end of the experiments, we also super-perfused the cells with 150 mM KCl extracellular solution to examine whether they show robust calcium responses, as confirmation of the imaged cells being healthy neurons.

Multi-electrode array recordings

To conduct spatially resolved recording of cortical activity during optogenetic excitation, we followed the approach by Khodagholy et al. [71]. A conducting and flexible microelectrode array called Neurogrid was adapted for mouse experiments. An array of 17 × 14 electrodes (electrode spacing: 250 μm) was placed on the scalp of anesthetized AAV9-treated mice following craniotomy. A T_1-weighted MRI scan showing the location of the BBB opening and the expected viral delivery was used as a guide for the Neurogrid placement. Local field potentials across the cortical surface were recorded before and during red light exposure. Neural spiking was recorded from each electrode independently, and was then integrated over time to calculate the average power at each cortical location. A linear interpolation was performed for non-recording electrodes to derive maps of cortical activity during “light off” and “light on” states. Spectral analysis was performed to establish the frequency content of neuronal activation, both throughout the stimulation period and in a temporally-resolved manner.

Fear conditioning test

A fear conditioning test was developed to assess the combined long-term effects of FUS treatment and optogenetic activation on fear perception. The test consisted of three phases, conducted on three successive days: 1) habituation, 2) conditioning, and 3) recall. During habituation, mice were placed into a transparent cylinder positioned on a conducting metallic grid. The red LED was fixed on the upper end of the cylinder, at a height of 160 mm. The distance between the mouse scalp and the LED varied between 130 and 150 mm during the course of the trials, due to mouse motion.

Mice were allowed to freely move within the chamber for 180 s. During conditioning, mice moved freely for 120 s. A 30-s tone was then heard, followed by a 2-s electric shock. This was followed by a 60-s idle period. The tone and the electric shock were repeated 3 times. The last shock was followed by a 30-s idle period, which completed the session. During recall, mice were initially given 180 s to move freely. Then, a 60 s tone was heard, which was not followed by a shock. A 30-s tone followed 60 s later, and was repeated one more time. The session ended immediately after the 3rd tone. A camera recorded side-view videos of mouse movement throughout the three sessions.

Animals were conditioned to experience a fearful response to the electric shock during conditioning, but were expected to learn that there is no shock coming during recall. The temporal component of the recall test was designed to test elements of working memory. As discussed earlier, three experimental groups were tested for fear conditioning: sham (n=11), FUS only (n=12), and FUS+AAV (n=18). Early histological studies showed no transduction of AAV in mice which were injected with AAV but not treated with FUS ("AAV only" group), and no ChrimsonR expression in brain regions not exposed to FUS (in the "FUS+AAV" group), thus we did not expect a behavioral effect in these mice. Therefore, we have not included an AAV only group in the experimental design of the behavioral study, in an effort to comply with the 3R principles. FUS treatments were targeted at multiple brain regions, such as the hippocampus, the thalamus, and the amygdala. All mice were exposed to red light (10% DC, 10 Hz PRF, 500 mA, and ~ 0.5-1 mW/mm^2 at the scalp) during the conditioning day.

Fearful responses were analyzed off-line. All videos were loaded onto ANY-maze (Wood Dale, IL, USA), and mouse motion was tracked throughout each session. Each frame was binarized as 0 (i.e., motion) or 1 (i.e., freezing). We first calculated the average freezing score per second for the entire course of the session. We then analyzed each tone separately, and found the average freezing time for each cohort, as a percentage of the total time

of the tone. Finally, we statistically compared the temporal variation in freezing across groups, to deduce the long-term behavioral changes following FUS treatment and optogenetic activation.

Statistics

All measurements are presented as mean ± standard deviation, unless otherwise stated. A non-parametric Kruskas-Wallis test was used to statistically compare freezing times across groups in the fear conditioning test, and also compare the BBB opening volume and contrast enhancement in the MRI processing. A two-sided t-test was used to compare the firing rates between red/blue light and baseline in electrophysiology measurements. A linear regression was performed in the freezing time data across tones, to deduce the temporal evolution of the freezing behavior. The slopes of the linear regression were statistically compared with a slopes t-test.

Conflicts of interest statement

The authors declare no competing financial interests.

Acknowledgements This study was supported by the NIH grant 5R01EB009041 and 5R01AG038961. The authors acknowledge constructive input from all members of the Ultrasound Elasticity Imaging Laboratory at Columbia University. We would like to thank Mu Yang, Ph.D., for her valuable assistance in the behavioral testing. We would also like to thank Gustavo Rodriguez, Ph.D., for advice on histology and cFos staining.

Supplementary information is available in the online version of the paper.

Author contributions A.N.P., S.A.H. and E.E.K. conceived the concept and designed the experiments. A.N.P. performed the experiments and analyzed the data; M.F.M. and N.K. performed the immunohistochemistry. S.A.H. performed the *in vivo* electrophysiology measurements. H.Y., J.N.G. and D.K.A. performed the multi-electrode array recordings. C.K.T. performed the Ca^{2+} imaging. M.F.M. performed the fear conditioning experiment. All authors discussed the results and approved the manuscript.

716 **Author information** Reprints and permissions information is available online. Readers are welcome to comment on
717 the online version of the paper. Correspondence and requests for materials should be addressed to E.E.K.
718 (ek2191@columbia.edu).

719

References

[1] Chen R, Romero G, Christiansen MG, Mohr A, Anikeeva P. Wireless magnetothermal deep brain stimulation. Science (1979) 2015;347:1477 LP – 1480.

[2] Gomez JL, Bonaventura J, Lesniak W, Mathews WB, Sysa-Shah P, Rodriguez LA, et al. Chemogenetics revealed: DREADD occupancy and activation via converted clozapine. Science (1979) 2017;357:503 LP – 507.

[3] Fan CH, Wei KC, Chiu NH, Liao EC, Wang HC, Wu RY, et al. Sonogenetic-Based Neuromodulation for the Amelioration of Parkinson's Disease. Nano Letters 2021;21:5967–76. https://doi.org/10.1021/acs.nanolett.1c00886.

[4] Ibsen S, Tong A, Schutt C, Esener S, Chalasani SH. Sonogenetics is a non-invasive approach to activating neurons in Caenorhabditis elegans. Nature Communications 2015;6:1–12. https://doi.org/10.1038/ncomms9264.

[5] Boyden ES, Zhang F, Bamberg E, Nagel G, Deisseroth K. Millisecond-timescale, genetically targeted optical control of neural activity. Nature Neuroscience 2005;8:1263–8. https://doi.org/10.1038/nn1525.

[6] Szobota S, Isacoff EY. Optical Control of Neuronal Activity. Annual Review of Biophysics 2010;39:329–48. https://doi.org/10.1146/annurev.biophys.093008.131400.

[7] Häusser M. Optogenetics: the age of light. Nature Methods 2014;11:1012–4. https://doi.org/10.1038/nmeth.3111.

[8] Adamantidis AR, Zhang F, Aravanis AM, Deisseroth K, de Lecea L. Neural substrates of awakening probed with optogenetic control of hypocretin neurons. Nature 2007;450:420–4. https://doi.org/10.1038/nature06310.

[9] Cardin JA, Carlén M, Meletis K, Knoblich U, Zhang F, Deisseroth K, et al. Targeted optogenetic stimulation and recording of neurons in vivo using cell-type-specific expression of Channelrhodopsin-2. Nature Protocols 2010;5:247–54. https://doi.org/10.1038/nprot.2009.228.

[10] Marshel JH, Kim YS, Machado TA, Quirin S, Benson B, Kadmon J, et al. Cortical layer-specific critical dynamics triggering perception. Science (1979) 2019;365:1–23. https://doi.org/10.1126/science.aaw5202.

[11] Rajasethupathy P, Sankaran S, Marshel JH, Kim CK, Ferenczi E, Lee SY, et al. Projections from neocortex mediate top-down control of memory retrieval. Nature 2015;526:653–9. https://doi.org/10.1038/nature15389.

[12] Redondo RL, Kim J, Arons AL, Ramirez S, Liu X, Tonegawa S. Bidirectional switch of the valence associated with a hippocampal contextual memory engram. Nature 2014;513:426–30. https://doi.org/10.1038/nature13725.

[13] Liu X, Ramirez S, Pang PT, Puryear CB, Govindarajan A, Deisseroth K, et al. Optogenetic stimulation of a hippocampal engram activates fear memory recall. Nature 2012;484:381–5. https://doi.org/10.1038/nature11028.

[14] Ramirez S, Liu X, Lin PA, Suh J, Pignatelli M, Redondo RL, et al. Creating a false memory in the hippocampus. Science (1979) 2013;341:387–91. https://doi.org/10.1126/science.1239073.

[15] Aravanis AM, Wang L-P, Zhang F, Meltzer LA, Mogri MZ, Schneider MB, et al. An optical neural interface: *in vivo* control of rodent motor cortex with integrated fiberoptic and optogenetic technology. Journal of Neural Engineering 2007;4:S143–56. https://doi.org/10.1088/1741-2560/4/3/S02.

[16] Zhang F, Prigge M, Beyrière F, Tsunoda SP, Mattis J, Yizhar O, et al. Red-shifted optogenetic excitation: A tool for fast neural control derived from Volvox carteri. Nature Neuroscience 2008;11:631–3. https://doi.org/10.1038/nn.2120.

[17] Lin JY, Knutsen PM, Muller A, Kleinfeld D, Tsien RY. ReaChR: A red-shifted variant of channelrhodopsin enables deep transcranial optogenetic excitation. Nature Neuroscience 2013;16:1499–508. https://doi.org/10.1038/nn.3502.

[18] Chuong AS, Miri ML, Busskamp V, Matthews GAC, Acker LC, Sørensen AT, et al. Noninvasive optical inhibition with a red-shifted microbial rhodopsin. Nat Neurosci 2014;17:1123–9. https://doi.org/10.1038/nn.3752.

[19] Chen S, Weitemier AZ, Zeng X, He L, Wang X, Tao Y, et al. Near-infrared deep brain stimulation via upconversion nanoparticle–mediated optogenetics. Science (1979) 2018;359:679–84. https://doi.org/10.1126/science.aaq1144.

[20] Chen R, Gore F, Nguyen QA, Ramakrishnan C, Patel S, Kim SH, et al. Deep brain optogenetics without intracranial surgery. Nature Biotechnology 2020 39:2 2020;39:161–4. https://doi.org/10.1038/s41587-020-0679-9.

[21] Wang S, Olumolade OO, Sun T, Samiotaki G, Konofagou EE. Noninvasive, neuron-specific gene therapy can be facilitated by focused ultrasound and recombinant adeno-associated virus. Gene Therapy 2015;22:104–10. https://doi.org/10.1038/gt.2014.91.

[22] Wang S, Kugelman T, Buch A, Herman M, Han Y, Karakatsani ME, et al. Non-invasive, Focused Ultrasound-Facilitated Gene Delivery for Optogenetics. Scientific Reports 2017;7:39955. https://doi.org/10.1038/srep39955.

[23] Wu X, Zhu X, Chong P, Liu J, Andre LN, Ong KS, et al. Sono-optogenetics facilitated by a circulationdelivered rechargeable light source for minimally invasive optogenetics. Proc Natl Acad Sci U S A 2019;116:26332–42. https://doi.org/10.1073/PNAS.1914387116/SUPPL_FILE/PNAS.1914387116.SM02.AVI.

[24] Klapoetke NC, Murata Y, Kim SS, Pulver SR, Birdsey-Benson A, Cho YK, et al. Independent optical excitation of distinct neural populations. Nature Methods 2014;11:338–46. https://doi.org/10.1038/nmeth.2836.

[25] Karakatsani ME, Kugelman T, Ji R, Murillo M, Wang S, Niimi Y, et al. Unilateral Focused Ultrasound-Induced Blood-Brain Barrier Opening Reduces Phosphorylated Tau from The rTg4510 Mouse Model. Theranostics 2019;9:5396–411. https://doi.org/10.7150/thno.28717.

[26] Ji R, Smith M, Niimi Y, Karakatsani ME, Murillo MF, Jackson-Lewis V, et al. Focused ultrasound enhanced intranasal delivery of brain derived neurotrophic factor produces neurorestorative effects in a Parkinson's disease mouse model. Scientific Reports 2019;9. https://doi.org/10.1038/s41598-019-55294-5.

[27] Olumolade OO, Wang S, Samiotaki G, Konofagou EE. Longitudinal Motor and Behavioral Assessment of Blood-Brain Barrier Opening with Transcranial Focused Ultrasound. Ultrasound in Medicine and Biology 2016;42:2270–82. https://doi.org/10.1016/j.ultrasmedbio.2016.05.004.

[28] Xu S, Ye D, Wan L, Shentu Y, Yue Y, Wan M, et al. Correlation Between Brain Tissue Damage and Inertial Cavitation Dose Quantified Using Passive Cavitation Imaging. Ultrasound in Medicine & Biology 2019. https://doi.org/10.1016/J.ULTRASMEDBIO.2019.07.004.

[29] Oda K, Vierock J, Oishi S, Rodriguez-Rozada S, Taniguchi R, Yamashita K, et al. Crystal structure of the red light-activated channelrhodopsin Chrimson. Nature Communications 2018 9:1 2018;9:1–11. https://doi.org/10.1038/s41467-018-06421-9.

[30] Lin C-Y, Hsieh H-Y, Chen C-M, Wu S-R, Tsai C-H, Huang C-Y, et al. Non-invasive, neuron-specific gene therapy by focused ultrasound-induced blood-brain barrier opening in Parkinson's disease mouse model. Journal of Controlled Release 2016;235:72–81. https://doi.org/10.1016/j.jconrel.2016.05.052.

[31] Wu CY, Fan CH, Chiu NH, Ho YJ, Lin YC, Yeh CK. Targeted delivery of engineered auditory sensing protein for ultrasound neuromodulation in the brain. Theranostics 2020;10:3546–61. https://doi.org/10.7150/thno.39786.

[32] Szablowski JO, Lee-Gosselin A, Lue B, Malounda D, Shapiro MG. Acoustically targeted chemogenetics for the non-invasive control of neural circuits. Nature Biomedical Engineering 2018;2:475–84. https://doi.org/10.1038/s41551-018-0258-2.

[33] Szablowski JO, Harb M. Focused ultrasound induced blood-brain barrier opening for targeting brain structures and evaluating chemogenetic neuromodulation. Journal of Visualized Experiments 2020;2020:e61352. https://doi.org/10.3791/61352.

[34] Yang Y, Pacia CP, Ye D, Zhu L, Baek H, Yue Y, et al. Sonothermogenetics for noninvasive and cell-type specific deep brain neuromodulation. Brain Stimulation 2021;14:790–800. https://doi.org/10.1016/j.brs.2021.04.021.

[35] Foust KD, Nurre E, Montgomery CL, Hernandez A, Chan CM, Kaspar BK. Intravascular AAV9 preferentially targets neonatal neurons and adult astrocytes. Nature Biotechnology 2009;27:59–65. https://doi.org/10.1038/nbt.1515.

[36] Thévenot E, Jordão JF, O'Reilly MA, Markham K, Weng YQ, Foust KD, et al. Targeted delivery of self-complementary adeno-associated virus serotype 9 to the brain, using magnetic resonance imaging-guided focused ultrasound. Human Gene Therapy 2012;23:1144–55. https://doi.org/10.1089/hum.2012.013.

[37] Li H, Heath JE, Trippett JS, Shapiro MG, Szablowski JO. Engineering Viral Vectors for Acoustically Targeted Gene Delivery. BioRxiv 2021:2021.07.26.453904. https://doi.org/10.1101/2021.07.26.453904.

[38] Weber-Adrian D, Kofoed RH, Silburt J, Noroozian Z, Shah K, Burgess A, et al. Systemic AAV6-synapsin-GFP administration results in lower liver biodistribution, compared to AAV1&2 and AAV9, with neuronal expression following ultrasound-mediated brain delivery. Scientific Reports 2021;11:1934. https://doi.org/10.1038/s41598-021-81046-5.

[39] Liguore WA, Domire JS, Button D, Wang Y, Dufour BD, Srinivasan S, et al. AAV-PHP.B Administration Results in a Differential Pattern of CNS Biodistribution in Non-human Primates Compared with Mice. Molecular Therapy 2019;27:2018–37. https://doi.org/10.1016/j.ymthe.2019.07.017.

[40] Bedbrook CN, Yang KK, Robinson JE, Mackey ED, Gradinaru V, Arnold FH. Machine learning-guided channelrhodopsin engineering enables minimally invasive optogenetics. Nature Methods 2019 16:11 2019;16:1176–84. https://doi.org/10.1038/s41592-019-0583-8.

[41] Chan KY, Jang MJ, Yoo BB, Greenbaum A, Ravi N, Wu WL, et al. Engineered AAVs for efficient noninvasive gene delivery to the central and peripheral nervous systems. Nature Neuroscience 2017 20:8 2017;20:1172–9. https://doi.org/10.1038/nn.4593.

[42] Broser M, Spreen A, Konold PE, Peter E, Adam S, Borin V, et al. NeoR, a near-infrared absorbing rhodopsin. Nature Communications 2020 11:1 2020;11:1–10. https://doi.org/10.1038/s41467-020-19375-8.

[43] Kaberniuk AA, Baloban M, Monakhov M V., Shcherbakova DM, Verkhusha V V. Single-component near-infrared optogenetic systems for gene transcription regulation. Nature Communications 2021 12:1 2021;12:1–12. https://doi.org/10.1038/s41467-021-24212-7.

[44] Liu HL, Hua MY, Yang HW, Huang CY, Chu PN, Wu JS, et al. Magnetic resonance monitoring of focused ultrasound/magnetic nanoparticle targeting delivery of therapeutic agents to the brain. Proc Natl Acad Sci U S A 2010;107:15205–10. https://doi.org/10.1073/pnas.1003388107.

[45] Guo Y, Lee H, Fang Z, Velalopoulou A, Kim J, Thomas M Ben, et al. Single-cell analysis reveals effective siRNA delivery in brain tumors with microbubble-enhanced ultrasound and cationic nanoparticles. Science Advances 2021;7:eabf7390. https://doi.org/10.1126/sciadv.abf7390.

[46] Karakatsani ME, Wang S, Samiotaki G, Kugelman T, Olumolade OO, Acosta C, et al. Amelioration of the nigrostriatal pathway facilitated by ultrasound-mediated neurotrophic delivery in early Parkinson's disease. Journal of Controlled Release 2019;303:289–301. https://doi.org/10.1016/J.JCONREL.2019.03.030.

[47] Melde K, Mark AG, Qiu T, Fischer P. Holograms for acoustics. Nature 2016;537:518–22. https://doi.org/10.1038/nature19755.

[48] Jiménez-Gambín S, Jiménez N, Benlloch JM, Camarena F. Holograms to Focus Arbitrary Ultrasonic Fields through the Skull. Physical Review Applied 2019;12:014016. https://doi.org/10.1103/PhysRevApplied.12.014016.

[49] Jimenez-Gambin S, Jimenez N, Pouliopoulos A, Benlloch JM, Konofagou EE, Camarena F. Acoustic holograms for bilateral blood-brain barrier opening in a mouse model. IEEE Transactions on Biomedical Engineering 2022;69:1359–68. https://doi.org/10.1109/TBME.2021.3115553.

[50] Anastasiadis P, Gandhi D, Guo Y, Ahmed A-K, Bentzen SM, Arvanitis C, et al. Localized blood–brain barrier opening in infiltrating gliomas with MRI-guided acoustic emissions–controlled focused ultrasound. Proceedings of the National Academy of Sciences 2021;118. https://doi.org/10.1073/PNAS.2103280118.

[51] Pouliopoulos AN, Bonaccorsi S, Choi JJ. Exploiting flow to control the in vitro spatiotemporal distribution of microbubble-seeded acoustic cavitation activity in ultrasound therapy. Physics in Medicine and Biology 2014;59:6941–57. https://doi.org/10.1088/0031-9155/59/22/6941.

[52] Pouliopoulos AN, Li C, Tinguely M, Garbin V, Tang M-X, Choi JJ. Rapid short-pulse sequences enhance the spatiotemporal uniformity of acoustically driven microbubble activity during flow conditions. J Acoust Soc Am 2016;140:2469–80. https://doi.org/10.1121/1.4964271.

[53] Morse S V, Pouliopoulos AN, Chan TG, Copping MJ, Lin J, Long NJ, et al. Rapid Short-pulse Ultrasound Delivers Drugs Uniformly across the Murine Blood-Brain Barrier with Negligible Disruption. Radiology 2019;291:459–66. https://doi.org/10.1148/radiol.2019181625.

[54] Todd N, Angolano C, Ferran C, Devor A, Borsook D, McDannold N. Secondary effects on brain physiology caused by focused ultrasound-mediated disruption of the blood–brain barrier. Journal of Controlled Release 2020;324:450–9. https://doi.org/10.1016/j.jconrel.2020.05.040.

[55] Scarcelli T, Jordão JF, O'reilly MA, Ellens N, Hynynen K, Aubert I. Stimulation of hippocampal neurogenesis by transcranial focused ultrasound and microbubbles in adult mice. Brain Stimulation 2014;7:304–7. https://doi.org/10.1016/j.brs.2013.12.012.

[56] Shin J, Kong C, Lee J, Choi BY, Sim J, Koh CS, et al. Focused ultrasound-induced blood-brain barrier opening improves adult hippocampal neurogenesis and cognitive function in a cholinergic degeneration dementia rat model. Alzheimer's Research & Therapy 2019;11:110. https://doi.org/10.1186/s13195-019-0569-x.

[57] Pouliopoulos AN, Kwon N, Jensen G, Meaney A, Niimi Y, Burgess MT, et al. Safety evaluation of a clinical focused ultrasound system for neuronavigation guided blood-brain barrier opening in non-human primates. Scientific Reports 2021;11:15043. https://doi.org/10.1038/s41598-021-94188-3.

[58] McMahon D, Mah E, Hynynen K. Angiogenic response of rat hippocampal vasculature to focused ultrasound-mediated increases in blood-brain barrier permeability. Scientific Reports 2018;8:12178. https://doi.org/10.1038/s41598-018-30825-8.

[59] Todd N, Zhang Y, Arcaro M, Becerra L, Borsook D, Livingstone M, et al. Focused ultrasound induced opening of the blood-brain barrier disrupts inter-hemispheric resting state functional connectivity in the rat brain. Neuroimage 2018;178:414–22. https://doi.org/10.1016/j.neuroimage.2018.05.063.

[60] Kobus T, Vykhodtseva N, Pilatou M, Zhang Y, McDannold N. Safety Validation of Repeated Blood-Brain Barrier Disruption Using Focused Ultrasound. Ultrasound Med Biol 2016;42:481–92. https://doi.org/10.1016/j.ultrasmedbio.2015.10.009.

[61] Choi JJ, Pernot M, Small SA, Konofagou EE. Noninvasive, transcranial and localized opening of the blood-brain barrier using focused ultrasound in mice. Ultrasound Med Biol 2007;33:95–104. https://doi.org/10.1016/j.ultrasmedbio.2006.07.018.

[62] Pouliopoulos AN, Jimenez DA, Frank A, Robertson A, Zhang L, Kline-Schoder AR, et al. Temporal Stability of Lipid-Shelled Microbubbles During Acoustically-Mediated Blood-Brain Barrier Opening. Frontiers in Physics 2020;8:137. https://doi.org/10.3389/fphy.2020.00137.

[63] Pouliopoulos ANN, Burgess MT, Konofagou EE. Pulse inversion enhances the passive mapping of microbubble-based ultrasound therapy. Applied Physics Letters 2018;113:044102.

[64] Choi JJ, Selert K, Vlachos F, Wong A, Konofagou EE. Noninvasive and localized neuronal delivery using short ultrasonic pulses and microbubbles. Proc Natl Acad Sci U S A 2011;108:16539–44. https://doi.org/10.1073/pnas.1105116108.

[65] Chen H, Konofagou EE. The size of blood-brain barrier opening induced by focused ultrasound is dictated by the acoustic pressure. J Cereb Blood Flow Metab 2014;34. https://doi.org/10.1038/jcbfm.2014.71.

[66] Wang S, Kugelman T, Buch A, Herman M, Han Y, Karakatsani ME, et al. Non-invasive, Focused Ultrasound-Facilitated Gene Delivery for Optogenetics. Scientific Reports 2017;7:39955. https://doi.org/10.1038/srep39955.

[67] Kügler S, Kilic E, Bähr M. Human synapsin 1 gene promoter confers highly neuron-specific long-term transgene expression from an adenoviral vector in the adult rat brain depending on the transduced area. Gene Therapy 2003 10:4 2003;10:337–47. https://doi.org/10.1038/sj.gt.3301905.

[68] Wu JW, Hussaini SA, Bastille IM, Rodriguez GA, Mrejeru A, Rilett K, et al. Neuronal activity enhances tau propagation and tau pathology in vivo. Nature Neuroscience 2016;19:1085–92. https://doi.org/10.1038/nn.4328.

[69] Hussaini SA, Kempadoo KA, Thuault SJ, Siegelbaum SA, Kandel ER. Increased Size and Stability of CA1 and CA3 Place Fields in HCN1 Knockout Mice. Neuron 2011;72:643–53. https://doi.org/10.1016/J.NEURON.2011.09.007.

[70] Kuehl-Kovarik MC, Partin KM, Magnusson KR. Acute dissociation for analyses of NMDA receptor function in cortical neurons during aging. Journal of Neuroscience Methods 2003;129:11–7. https://doi.org/10.1016/S0165-0270(03)00196-1.

[71] Khodagholy D, Gelinas JN, Buzsáki G. Learning-enhanced coupling between ripple oscillations in association cortices and hippocampus. Science (1979) 2017;358:369–72. https://doi.org/10.1126/SCIENCE.AAN6203.

Figures

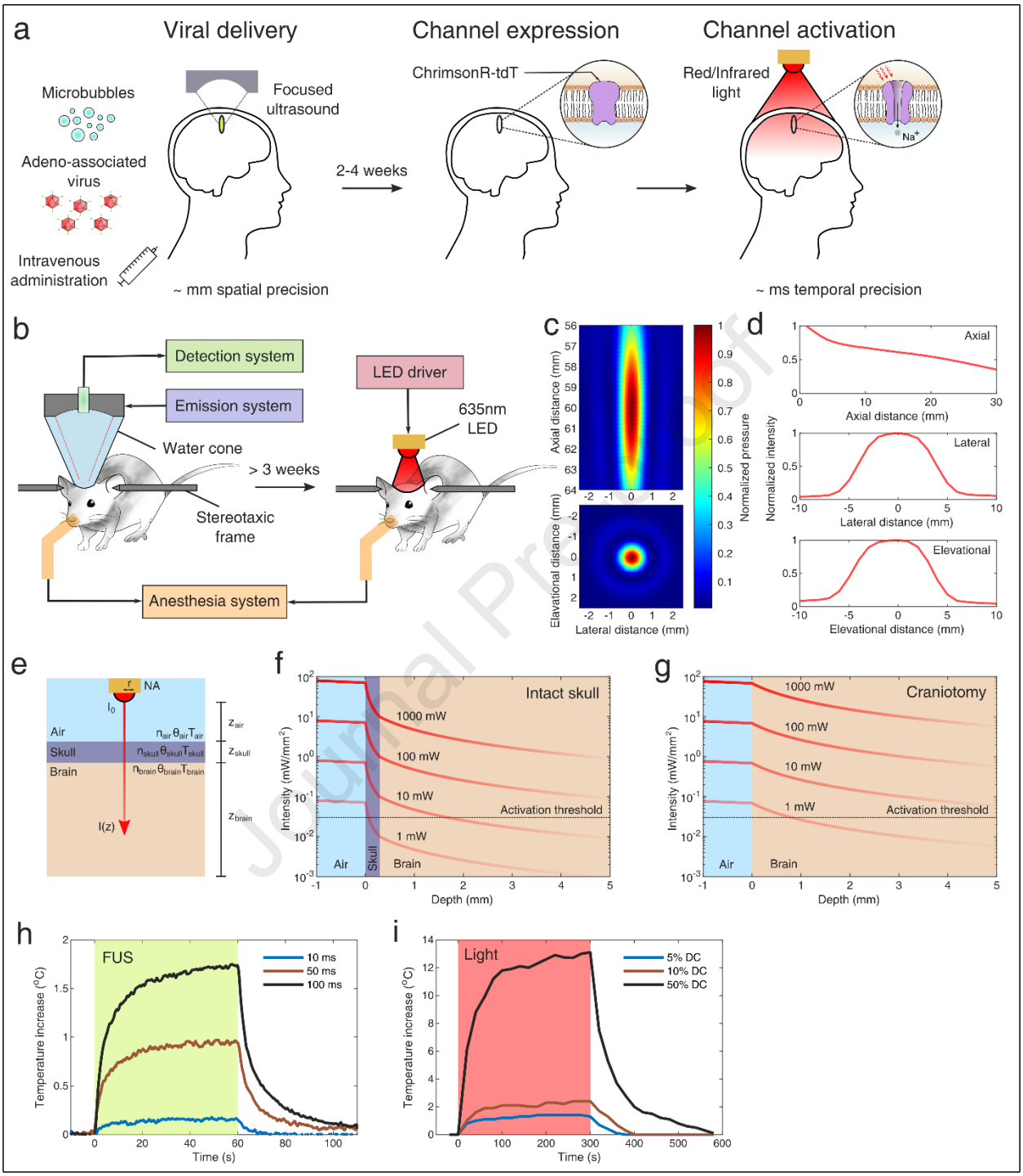

Fig. 1 | Non-invasive optogenetics with FUS-mediated gene delivery and red-light activation. a, Concept of the proposed method. Application of FUS in conjunction with systemically administered microbubbles allows targeted opening of the BBB and localized sub-mm expression of red-shifted opsins, e.g. ChrimsonR. Exposure to red light activates light-sensitive channels with sub-ms temporal precision Note: a human head is included only for illustration purposes, but no humans were included in this *in vivo* study. **b**, Experimental setup for non-invasive optogenetics in

mice. A single-element focused ultrasound transducer produced therapeutic pulses aimed at the hippocampal area of anesthetized mice. Real-time acoustic monitoring was performed with a passive cavitation detector. Following viral transduction and ChrimsonR expression, mice were exposed to red-light either under anesthesia or in free field. **c**, Ultrasonic focal volume calibration using a bullet hydrophone. The measured focal volume dimensions were 1 mm × 1 mm × 7.5 mm. Axial distance represented the distance from the surface of the FUS transducer. **d**, LED calibration using a photometer. Normalized light intensity along the axial, lateral, and elevational directions. **e**, Three-compartmental analytical model of red light propagation through air, skull, and skin. **f**, Light intensity over depth with intact skull for different emitted optical power. **g**, Light intensity over depth with craniotomy for different emitted optical power. **h**, Skull heating induced by ultrasound exposure *in vivo* using different pulse length. **i**, Skull heating induced by light exposure using different duty cycle.

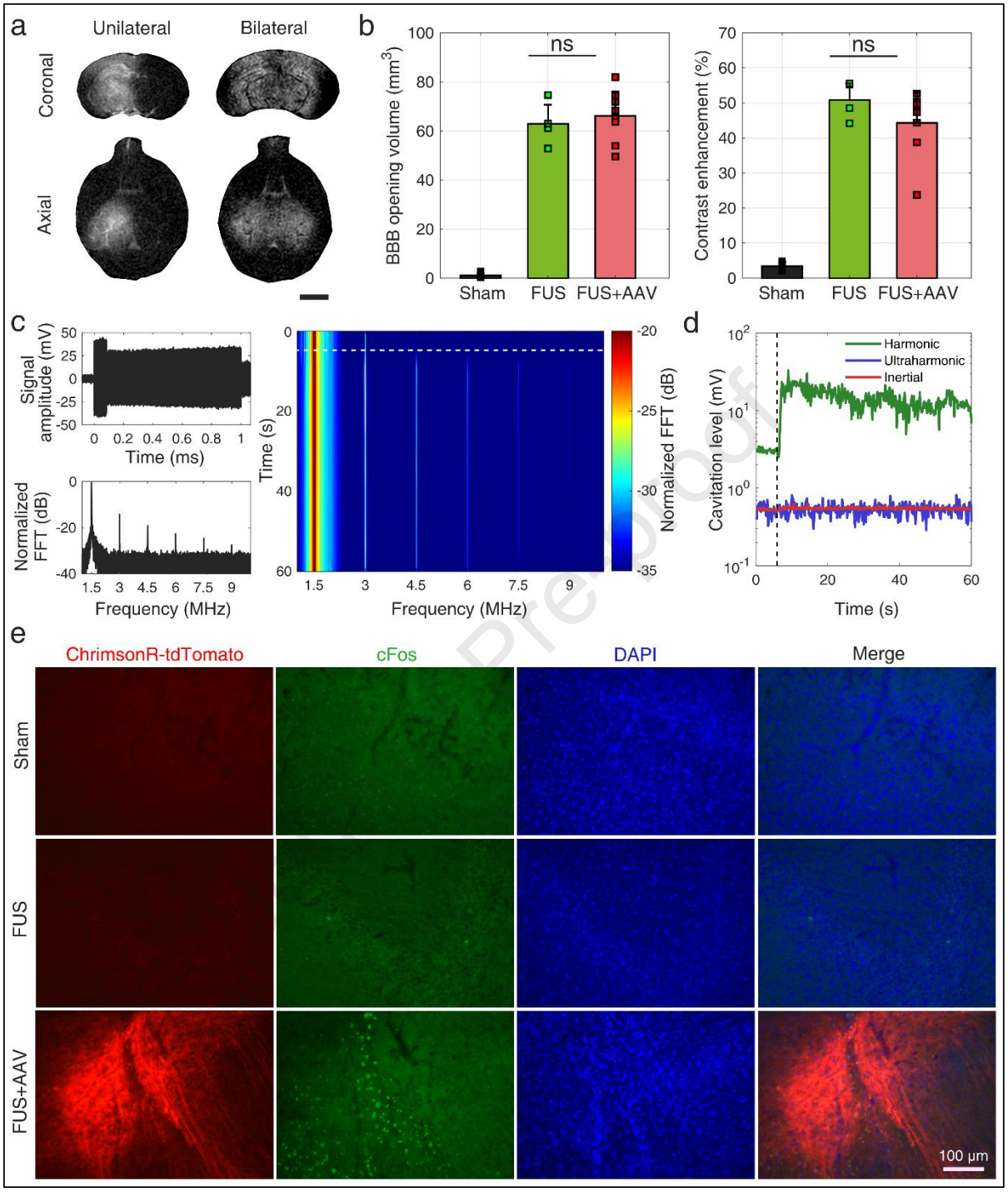

Fig. 2 | Non-invasive, targeted, and acoustically-monitored viral delivery permits remote and selective neuronal activation. a, Coronal and axial contrast-enhanced T_1-weighted MRI scans confirming BBB opening in the targeted areas. **b**, BBB opening volume and contrast enhancement across the experimental groups. **c**, Time- and frequency-domain of microbubble acoustic emission monitored in real-time. **d**, Cavitation level evolution during BBB opening. Cavitation doses across experimental groups. **e**, Neuronal activation in proximity to ChrimsonR expressing brain regions confirmed with cFos staining (example from hippocampal areas). ns: non-significant, Kruskas-Wallis test.

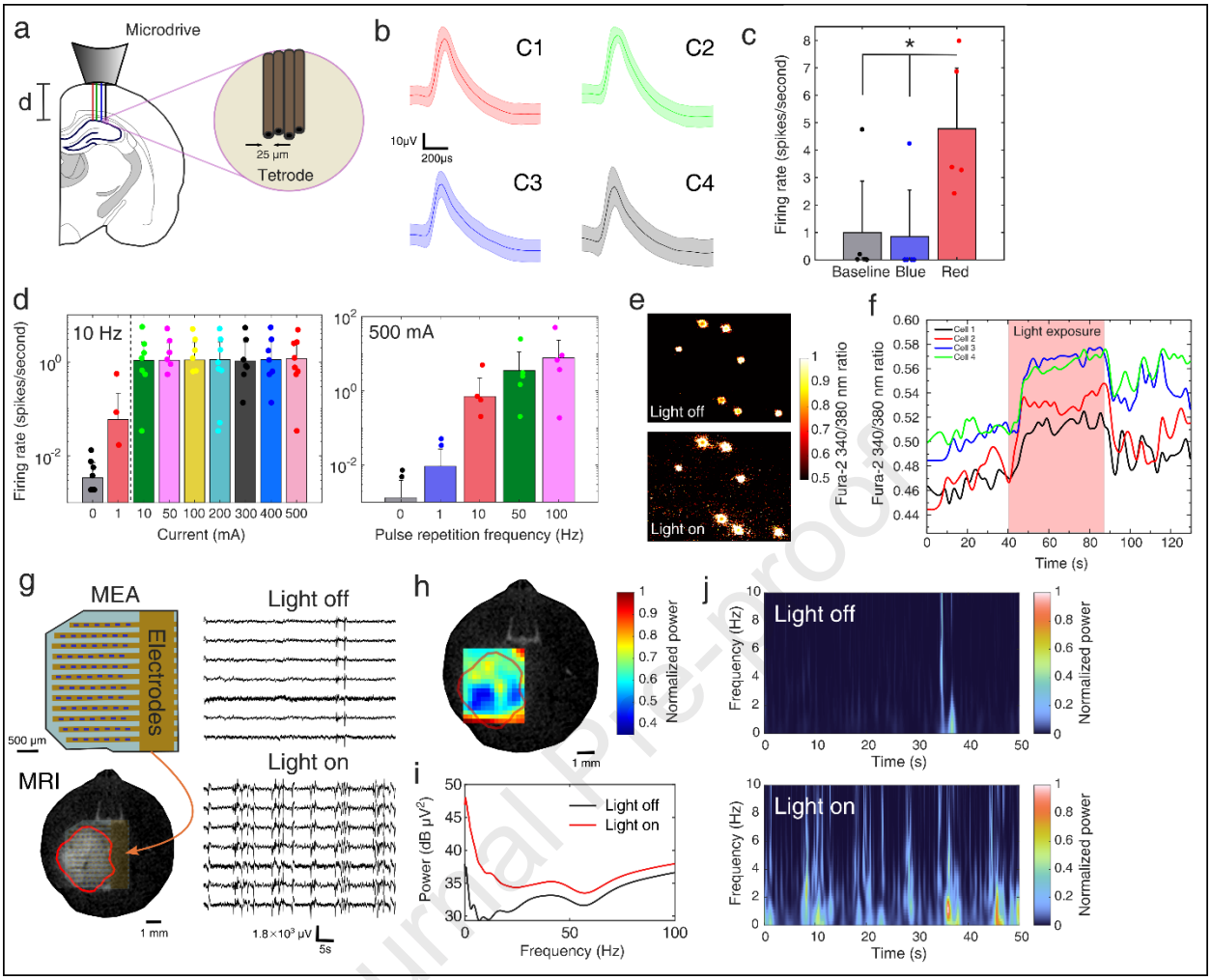

Fig. 3 | Brain activity elicited during illumination. a, *In vivo* electrophysiology in anesthetized mice using implanted tetrodes made of 90% Pt/10% Ir at a recording depth d. **b**, Representative spikes detected recorded across 4 channels of a tetrode. **c**, Neuronal firing rate at baseline, during blue-light and during red-light illumination. **d**, Neuronal firing rate dependence on light intensity and pulse repetition frequency (light pulse length: 10ms). **e**, Ca^{2+} imaging of dissociated ChrimsonR^{+} neurons in the "light off" and "light on" state. **f**, Fura-2 340/380 nm ratio in ChrimsonR^{+} neurons at baseline and during light exposure. **g**, Multi-electrode array measurements. The array was placed above the BBB opened area based on the T_1-weighted MRI scan. Time-domain signal was recorded at baseline and during 1-Hz light exposure. The MEA illustration is representative and does not depict the actual distribution of the 17 × 14 electrodes. The electrode spacing was 250 µm. **h**, Two-dimensional power map of cortical activity during 1-Hz light exposure. **i**, Spectral power of neuronal activity averaged across all channels at baseline and during 1-Hz light exposure. **j**, Spectrograms of neuronal activity averaged across all channels at baseline and during 1-Hz light exposure. *: $p<0.05$, two-sided t-test.

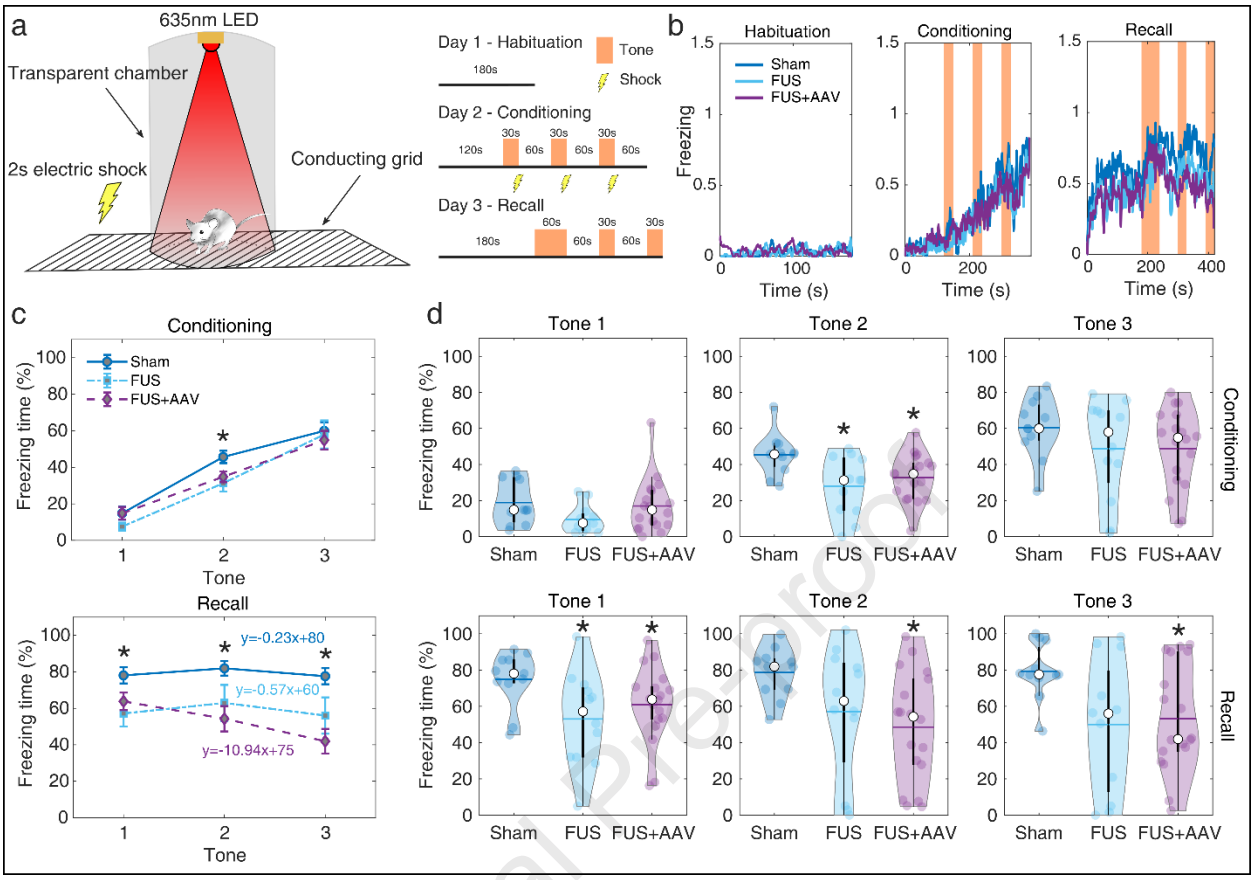

964

965 **Fig. 4 | Fear conditioning following FUS-mediated gene delivery and red-light stimulation. a**, Fear conditioning
966 experiment. Experimental setup and timeline. Day 1: Habituation; Day 2: Conditioning; Day 3: Recall. **b**, Freezing
967 score over time across experimental groups. **c**, Freezing time (% of tone duration) across all tones and across
968 experimental groups (median ± S.E.). **d**, Freezing time (% of tone duration) for all mice tested across all tones and
969 across experimental groups. Post-hoc analysis is shown between sham and the FUS/FUS+AAV groups. *: $p<0.05$,
970 Kruskas-Wallis test. Slopes were statistically compared with a slopes t-test.

971

972

Non-invasive optogenetics with ultrasound-mediated gene delivery and red-light excitation

Highlights

- Optogenetics is typically an invasive and spatially-restricted procedure
- Focused ultrasound treatment and red light exposure can replace invasive procedures
- The proposed approach allows non-invasive viral delivery and neuronal excitation *in vivo*
- Neuronal activation was confirmed through 1D and 2D electrophysiology *in vivo*
- Freezing behavior was affected in mice treated with focused ultrasound

Non-invasive optogenetics with ultrasound-mediated gene delivery and red-light excitation

Declaration of Interest

The authors declare no competing financial interests.